Analytic continuation-free Green's function approach to correlated electronic structure calculations

A. Östlin,[1] L. Vitos,[2,3,4] and L. Chioncel[5,1]

[1]*Theoretical Physics III, Center for Electronic Correlations and Magnetism, Institute of Physics, University of Augsburg, D-86135 Augsburg, Germany*

[2]*Department of Materials Science and Engineering, Applied Materials Physics, KTH Royal Institute of Technology, SE-10044 Stockholm, Sweden*

[3]*Department of Physics and Astronomy, Division of Materials Theory, Uppsala University, Box 516, SE-75120 Uppsala, Sweden*

[4]*Research Institute for Solid State Physics and Optics, Wigner Research Center for Physics, P.O. Box 49, H-1525 Budapest, Hungary*

[5]*Augsburg Center for Innovative Technologies, University of Augsburg, D-86135 Augsburg, Germany*

(Received 4 August 2017; revised manuscript received 18 September 2017; published 29 September 2017)

We present a charge self-consistent scheme combining density functional and dynamical mean field theory, which uses Green's functions of multiple-scattering type. In this implementation, the many-body effects are incorporated into the Kohn-Sham iterative scheme without the need for the numerically ill-posed analytic continuation of the Green's function and of the self-energy, which was previously a bottleneck in multiple-scattering-type Green's function approaches. This is achieved by producing the Kohn-Sham Hamiltonian in the subspace of correlated partial waves and allows to formulate the Green's function directly on the Matsubara axis. The spectral moments of the Matsubara Green's function enable us to put together the real-space charge density, therefore, the charge self-consistency can be achieved. Our results for the spectral functions (density of states) and equation-of-state curves for transition-metal elements Fe, Ni, and FeAl compound agree very well with those of Hamiltonian-based LDA+DMFT implementations. The current implementation improves on numerical accuracy, compared to previous implementations where analytic continuation was required at each Kohn-Sham self-consistent step. A minimal effort aside from the multiple-scattering formulation is required, and the method can be generalized in several ways that are interesting for applications to real materials.

DOI: 10.1103/PhysRevB.96.125156

I. INTRODUCTION

Density functional theory (DFT) [1] in conjunction with the Kohn-Sham scheme [2] and the local density approximation (LDA) [3], or the generalized gradient approximation (GGA) [4], to the exchange-correlation potential has shown great success in the computation of ground-state properties of real materials. However, the method cannot correctly describe materials where electronic correlations are important, such as the Mott insulators, 3*d* transition metals, and lanthanides. One successful approach to improve on the description of the electronic structure of strongly correlated materials is to merge DFT with dynamical mean field theory (DMFT) [5–8]. Within DMFT the complicated many-body lattice problem is mapped self-consistently into a single quantum impurity hybridized with an effective bath. Nowadays, impurity problems are efficiently solved by various many-body techniques. Hence, DMFT developed into a comprehensive, nonperturbative and thermodynamically consistent theoretical framework for the investigation of correlated electrons on the lattice. The combination of DMFT and DFT, referred to as LDA+DMFT and GGA+DMFT, respectively, has now become the state-of-the-art method to study correlated materials [8,9].

During the last decade, various LDA+DMFT implementations have been proposed. The early implementations employed a two-step procedure: in the first step the LDA problem was solved using an effective one-particle Kohn-Sham Hamiltonian and the single-particle wave functions (Kohn-Sham basis set) were integrated into the density functional variational approach. The corresponding Green's function was then obtained using the spectral representation of the Kohn-Sham Hamiltonian. In the second step, the interaction problem was treated, i.e., the low-energy effective Hamiltonian was formulated within a Wannier-type basis obtained through downfolding or, alternatively, by a suitable combination of Kohn-Sham basis sets. This low-energy Hamiltonian was solved using DMFT. Some of the initial LDA+DMFT implementations kept the effective Kohn-Sham potential fixed, and considered only the self-consistency of the local self-energy. Therefore, in these approaches the effect of the self-energy on the electronic charge was neglected. Inserting the self-energy back into the Kohn-Sham iterative scheme allows one to converge towards self-consistency in both the self-energy and charge. Several different basis sets have been used as a framework for LDA+DMFT Hamiltonian-based implementations, for example, pseudopotential plane waves [10–19], muffin-tin orbitals [20–27], and augmented plane waves [28–33], as well as mesh functions [34]. These procedures follow the spirit of the spectral density functional theory (SDFT) proposed by Savrasov and Kotliar [20], in which a self-consistent solution of the Dyson equation is sought. This leads to a quasiparticle Schrödinger (or Dirac) equation with a non-Hermitian part in the Hamiltonian.

An elegant way to avoid the difficulties involved in dealing with the non-Hermitian Hamiltonian in the SDFT formulation of LDA+DMFT is provided by the multiple-scattering method based on Green's functions. Green's function methods have the attractive feature that they can be easily used to treat systems such as surfaces, defects, and impurities [35,36]. They can also be employed in connection with the coherent potential approximation (CPA) to study substitutional disorder [37]. Common to many Green's function methods is the problem that the electronic eigenvalue problem is formulated as an *energy-dependent* secular equation, from which it is difficult

to extract the energy bands. Therefore, the charge density and the total energy, the relevant quantities for the DFT calculation, are obtained by integration of the Green's function along contours in the complex energy plane [38]. Some of the first charge self-consistent implementations of LDA+DMFT with a Green's function formulation of the Kohn-Sham DFT were implemented within the exact muffin-tin orbitals (EMTO) method [39] and the Korringa-Kohn-Rostoker (KKR) method [40,41].

One of the major goals of any self-consistent LDA+DMFT computation is to answer the question of how the effects of electronic correlation modify the equilibrium properties, like lattice parameters and bulk modulus, beyond the LDA. It is hence necessary to calculate accurate total energies within LDA+DMFT, from which the equilibrium quantities can be derived. Several of the ground-state quantities and spectral properties have already been discussed [42,43] within the Hamiltonian framework. Despite the many successes of Green's function based LDA+DMFT methods [41], several numerical difficulties still remain for total-energy calculations. When the Green's function based LDA+DMFT scheme is executed in practice, Padé approximants [44] (rational polynomials) are used to pass Green's functions from the complex energy contour to the Matsubara frequencies, and to return with the self-energy from the Matsubara frequencies back to the complex contour. Aside from being sensitive to numerical noise [45], Padé approximants may miss important features, that can only be captured by resummation of the continued fraction to infinite order [45–47]. In recent years, some methods have been proposed in order to improve on the original Padé approximation technique [48–50] to the analytic continuation of the Green's function, but as of yet no fully satisfactory solution to this problem exists. Such numerical problems are presently a bottleneck for an accurate and stable self-consistent Green's function based LDA+DMFT method that can produce reliable total energies.

The success of LDA+DMFT consists in its ability to produce a self-consistent, numerically manageable approximation for the spectral function and for lattice properties at equilibrium. It is desirable that LDA+DMFT developments be exact *in principle*, and that even approximate perturbative solvers should give good results, irrespective of whether a Hamiltonian or Green's function method is used. For these reasons, it is essential to pursue alternative methods that improve on the numerical accuracy. In general, for a Green's function formulation of the LDA+DMFT the knowledge of the noninteracting Green's function along the imaginary axis is required. Consequently, our primary objective of this paper is to describe an approach which yields an accurate Green's function in Matsubara frequencies which can be used in the DMFT part and, at the same time, in constructing the charge density.

Our method makes the analytic continuation during the self-consistent Kohn-Sham iterations unnecessary. The key observation that triggered this method development is that the charge density is the only ingredient needed to close the Kohn-Sham self-consistent loop. The charge density *difference* between correlated and noncorrelated calculations, evaluated on the imaginary Matsubara axis, is taken as the correction on the DFT level charge density. Quantities such as eigenvalues, Green's functions, and self-energies are only auxiliary quantities in this respect. In the method zMTO+DMFT presented here, the Green's function in Matsubara frequencies is evaluated from the LMTO eigenstates, i.e., in the basis of linearized partial waves. The choice to take the character z in the denomination zMTO+DMFT is to remind of the fact that the Green's functions in DFT are usually computed along a general complex contour mesh, i.e., $G(z)$, for a given muffin-tin potential. We implemented this scheme starting from our previous EMTO+DMFT method [39], which has been successfully used to study correlated systems, such as bulk $3d$ and $4d$ transition metals and compounds [39,51–53], and magnetic heterostructures [54,55]. For the future the method can be used to investigate, e.g., complex transition metals [56] and stacking faults in f-electron materials [57]. The use of a Green's function method opens the possibility to study systems that deviate from perfect crystalline conditions, such as alloys and surfaces. The current method employs the spherical approximation for the effective Kohn-Sham potential and total energy, which makes it suitable primarily for the close-packed systems. In the future, we plan to implement the full-charge density (FCD) [58] technique for the total energy in the correlated regime. However, such an extension will not affect the way the correlation effects are included here and will become significant only when studying anisotropic lattice deformations at the DMFT level.

The paper is organized as follows: Sec. II gives an overview of the muffin-tin formalism for the solution of the Kohn-Sham equations. Section III presents the charge self-consistent implementation, followed by results in Sec IV. A conclusion and outlook is given in Sec. V.

II. OVERVIEW OF THE MUFFIN-TIN FORMALISM

Muffin-tin based methods have in common that they partition space into spherical *muffin tins*, centered around the ions in the lattice, and the *interstitial*, the area outside of the muffin tins. Inside the muffin tins the effective potential is assumed to be spherically symmetric, while it is taken to be constant in the interstitial. The Kohn-Sham equations are solved separately within these regions, and the solution for the entire space is found by imposing boundary conditions between the muffin tins and the interstitial. The algebraic formulation of the matching conditions takes the form of a secular equation, which is in general energy dependent. Section II A describes this concept for the EMTO method. Section II B briefly reviews the concept of basis function linearization, which is important for the construction of the correlated orbitals in this work.

A. Charge density and the complex contour Green's function in the EMTO basis set

Within the muffin-tin formalism, the effective Kohn-Sham potential $V^{\sigma}_{\rm eff}(\mathbf{r})$ (σ denotes the spin) in the single-electron Kohn-Sham equations, labeled by state index j,

$$\left[\nabla^2 - V^{\sigma}_{\rm eff}(\mathbf{r})\right]\Psi^{\sigma}_j(\mathbf{r}) \;=\; \epsilon^{\sigma}_j\,\Psi^{\sigma}_j(\mathbf{r}), \tag{1}$$

is approximated by spherical muffin-tin wells centered at lattice sites $\mathbf{R}$. The exchange-correlation part of $V^{\sigma}_{\rm eff}(\mathbf{r})$ will in

the following always be approximated by the spin-polarized LDA, and we will from now on suppress the spin index for simplicity. For the EMTO basis set [59–62], the one-electron wave functions are expanded in exact muffin-tin orbitals $\bar{\psi}^a_{RL}$,

$$\Psi_j(\mathbf{r}) = \sum_{RL} \bar{\psi}^a_{RL}(\epsilon_j,\mathbf{r}_R) v^a_{RL,j}, \tag{2}$$

where $L \equiv (l,m)$ denotes the orbital and azimuthal quantum numbers, respectively, and $\mathbf{r}_R \equiv r_R \hat{r}_R = \mathbf{r} - \mathbf{R}$, where the vector notation for the index R has been omitted. The superscript a denotes the screening parameter. The orbitals $\bar{\psi}^a_{RL}$ are linear combinations of partial waves $\phi^a_{LR}(r_R)$, which are normalized solutions of the radial Schrödinger eqution inside the muffin tins with spherical potential $V_{\text{eff}}(r_R)$,

$$\frac{\partial^2 r_R \phi_{Rl}(z,r_R)}{\partial r_R^2} = \left[\frac{l(l+1)}{r_R^2} + V_{\text{eff}}(r_R) - z\right] r_R \phi_{Rl}(z,r_R), \tag{3}$$

and of the solutions in the interstitial region [62]. The angular momentum sum in Eq. (2) can in practice be truncated at $l_{\max} = 3$, making the basis minimal. Since the orbitals are centered around the lattice sites R, the basis is "local", making it suitable as a basis for correlated orbitals within DMFT. The coefficients $v^a_{RL,j}$ are determined from the condition that the expansion should fulfill Eq. (1) in all space, i.e., the orbitals should be everywhere continuous and have no derivative discontinuities (kinks) anywhere. In the EMTO formalism, this leads to the kink-cancellation equation

$$K^a_{RL,R'L'}(\epsilon_j) v^a_{RL,j} = 0 \tag{4}$$

which is equivalent to the KKR tail cancellation equation [62], written in a screened representation. The quantity $K^a_{RL,R'L'}(\epsilon_j)$ defines the kink matrix for an arbitrary complex energy z and has the form

$$K^a_{RL,R'L'}(z) \equiv a\delta_{RR'}\delta_{LL'} D^a_{RL}(z) - a S^a_{RL,R'L'}(z). \tag{5}$$

$D^a_{RL}(z)$ denotes the EMTO logarithmic derivative function [60,61], and $S^a_{RL,R'L'}(z)$ is the slope matrix [63]. Note that Eq. (4) is an *energy-dependent* secular equation, which allows one to determine the eigenvalues ϵ_j. These are obtained using numerical search algorithms for the roots of the secular determinant along the real energy axis. To simplify the notation further, we suppress the index for the screening parameter a.

For translation-invariant systems, the index R runs over the atoms in the primitive cell only, and the Fourier transformation of Eq. (5) produces a matrix equation in the reciprocal space:

$$\sum_{R''L''} K_{R'L',R''L''}(\mathbf{k},z) g_{R''L'',RL}(\mathbf{k},z) = \delta_{R'R}\delta_{L'L} \tag{6}$$

that is solved using Green's function methods. Accordingly, the path operator $g_{R''L'',RL}(\mathbf{k},z)$ is the unique solution of Eq. (6) [the inverse of the kink matrix $K_{R'L',R''L''}(\mathbf{k},z)$] that fulfills the combination of lattice symmetry and boundary conditions. The elements of the kink matrix are constructed from the Bloch wave vector ($\mathbf{k}$) dependent slope matrix [62]. Since the energy derivative of the kink matrix $\dot{K}_{RL,R'L'}(\mathbf{k},z)$ gives the overlap matrix for the EMTO basis set [63], these are used to normalize the path operator $g_{R''L'',RL}(\mathbf{k},z)$ and construct the matrix elements of the EMTO Green's function [60,61]

$$G_{RL,R'L'}(\mathbf{k},z) = \sum_{R''L''} g_{RL,R''L''}(\mathbf{k},z)\dot{K}_{R''L'',R'L'}(\mathbf{k},z) - \delta_{RR'}\delta_{LL'} I_{RL}(z), \tag{7}$$

where $I_{RL}(z)$ accounts for the unphysical poles of $\dot{K}_{RL,R'L'}(z)$ [61,62]. The total number of states at the Fermi level E_F is obtained as

$$N(E_F) = \frac{1}{2\pi i} \sum_{RL} \oint \sum_{\mathbf{k}} G_{RL,RL}(\mathbf{k},z)\, dz, \tag{8}$$

where the energy integral is carried out on a complex contour that cuts the real axis below the bottom of the valence band and at E_F. The $\mathbf{k}$ summation is performed over the Brillouin zone (BZ).

To close the Kohn-Sham self-consistency scheme requires the computation of the charge density. Within the EMTO method this is achieved through the real-space path operator [corrected for unphysical poles similarly as in Eq. (7) [62]] integrated over the same complex contour that is used to determine E_F:

$$n(\mathbf{r}) = \sum_R n_R(\mathbf{r}_R); \quad n_R(\mathbf{r}_R) = \sum_L n_{RL}(r_R) Y_L(\hat{r}_R),$$
$$n_{RL}(r_R) = \frac{1}{2\pi i} \oint \sum_{L',L''} C_{LL'L''} Z_{Rl''}(z,r_R) \times g_{RL'',RL'}(z) Z_{Rl'}(z,r_R) dz, \tag{9}$$

where $C_{L'LL''}$ is a real Gaunt number. Equation (9) is valid within the muffin-tin spheres and for $l \leqslant l_{\max}$, and $Z_{Rl}(z,r_R) = N_{Rl}(z)\phi_{Rl}(z,r_R)$, where $N_{Rl}(z)$ is a normalization function [61,62]. The specific set of real harmonics is denoted by $Y_L(\hat{r}_R)$.

B. Charge density and the Matsubara Green's function in the LMTO basis set

An alternative solution of Eq. (1) is obtained by the linearized muffin-tin orbitals (LMTO) [64,65] method. The same muffin-tin shape is used for the potentials as in the EMTO method, but with the additional approximation that the interstitial region is neglected, leading to the atomic sphere approximation (ASA). The LMTOs χ^γ_{RL} are constructed from the partial wave solutions ϕ_{Rl} inside the muffin-tin spheres, computed at an arbitrary energy $\epsilon_{Rl\nu}$ (commonly chosen as the center of gravity of the occupied part of the band), and from the energy derivative of the partial wave $\dot{\phi}_{Rl} = \partial\phi_{Rl}/\partial\epsilon|_{\epsilon=\epsilon_{Rl\nu}}$, viz.,

$$\chi^\gamma_{RL}(\mathbf{r}_R) = \phi_{Rl}(\mathbf{r}_R) + \sum_{R'L'} \dot{\phi}_{R'l'}(\mathbf{r}_R) h^\gamma_{R'L',RL}(\mathbf{k}). \tag{10}$$

The omitted energy argument of the partial wave ϕ_{Rl} means that the function is evaluated at an energy $\epsilon_{Rl\nu}$. In Eq. (10), $h^\gamma_{R'L',RL}(\mathbf{k})$ is defined as

$$h^\gamma_{R'L',LR}(\mathbf{k}) \equiv H^\gamma_{R'L',LR}(\mathbf{k}) - \epsilon_{Rl\nu}\delta_{L'L}\delta_{R'R}, \tag{11}$$

where $H^{\gamma}_{R'L',RL}(\mathbf{k})$ is the Kohn-Sham Hamiltonian in the so-called nearly orthogonal γ-representation [65,66], viz.,

$$H^{\gamma}_{RL,R'L'}(\mathbf{k}) = C_{Rl}\delta_{L'L}\delta_{R'R} + \sqrt{\Delta_{Rl}}S^{\gamma}_{RL,R'L'}(\mathbf{k})\sqrt{\Delta_{R'l'}}, \tag{12}$$

where $S^{\gamma}_{RL,R'L'}$ are the LMTO structure constants, and the potential parameters C_{Rl} and Δ_{Rl} are computed from the partial waves ϕ_{Rl} according to the prescription given in Ref. [65]. With the energy-independent LMTO basis functions [Eq. (10)], the lattice wave function (i.e., the linear muffin-tin wave function)

$$\Psi_j(\mathbf{r}) = \sum_{RL} \chi^{\gamma}_{RL}(\mathbf{r}_R)u_{RL,j} \tag{13}$$

follows the *energy-independent* eigenvalue problem

$$H^{\gamma}_{R'L',RL}(\mathbf{k})u_{RL,j}(\mathbf{k}) = \epsilon_j(\mathbf{k})u_{RL,j}(\mathbf{k}), \tag{14}$$

where the Hamiltonian eigenvalues $\epsilon_j(\mathbf{k})$ provide the band structure, and the eigenvectors $u_{RL,j}(\mathbf{k})$ contain Bloch vector specific information.

1. Moments from the LMTO eigenstates and complex contour

Once the LMTO Hamiltonian has been diagonalized [Eq. (14)], the energy moments can be evaluated as

$$\mathcal{M}^{q}_{Rl} \equiv \sum_{j\mathbf{k}}^{occ.}[\epsilon_j(\mathbf{k}) - \epsilon_{Rlv}]^q \sum_{L} |u_{RL,j}(\mathbf{k})|^2, \tag{15}$$

where the $q = 0$ and 1 moments correspond to the orbitals' occupation and one-electron energies, respectively. Note that the moments computed with the help of Eq. (15) are along the real energy axis.

To make contact with DMFT, we point out that the LMTO method has been already used to construct Green's functions: either from the potential parameters directly or from the Lehmann (eigenvalue) representation [24,36,65]

$$G_{RL,R'L'}(z) = \sum_{j\mathbf{k}} \frac{u_{RL,j}(\mathbf{k})[u_{R'L',j}(\mathbf{k})]^{\dagger}}{z - \epsilon_j(\mathbf{k})}. \tag{16}$$

The energy moments can then be computed along a similar complex contour as in the EMTO method [36], using the site and orbital diagonal part of the Green's function $(R'L') \equiv (RL)$, viz.,

$$\mathcal{M}^{q}_{Rl} = \frac{1}{2\pi i}\oint \sum_{m=-l}^{l} (z - \epsilon_{Rlv})^q G_{RL,RL}(z)dz, \tag{17}$$

where we remind the reader of the definition $L \equiv (l,m)$. The eigenvalue summation done in Eq. (15) is now replaced with the complex contour integration (17). The knowledge of the moments and the partial waves allows the computation of the charge density [36,65], viz.,

$$\begin{aligned} n_{Rl}(r_R) = {} & \mathcal{M}^0_{Rl}|\phi_{Rl}(r_R)|^2 + \mathcal{M}^2_{Rl}|\dot{\phi}_{Rl}(r_R)|^2 \\ & + 2\mathcal{M}^1_{Rl}\phi_{Rl}(r_R)\dot{\phi}_{Rl}(r_R) \\ & + \mathcal{M}^2_{Rl}\phi_{Rl}(r_R)\ddot{\phi}_{Rl}(r_R), \end{aligned} \tag{18}$$

and the DFT self-consistency loop can be closed.

Note that one advantage of the LMTO Green's function over a multiple-scattering Green's function is that its spectrum is discrete and upwards bound, i.e., it does not contain the free-electron continuum [67].

2. Moments from Matsubara LMTO Green's function

Equation (16) can be also defined for the Matsubara frequencies $i\omega_n = (2n+1)i\pi T$, where $n = 0, \pm 1, \ldots$, and T is the temperature. Pourovskii *et al.* [24], showed recently that the LMTO zeroth-energy moments can be extracted also from the imaginary frequency domain by standard Matsubara summation [68], viz.,

$$\mathcal{M}^0_{Rl} = T\sum_{n}\sum_{m=-l}^{l}\sum_{\mathbf{k}} G_{RL,RL}(\mathbf{k},i\omega_n)e^{i\omega_n 0^+} \tag{19}$$

with the $\mathbf{k}$-resolved Green's function given by the Lehmann representation

$$G_{RL,R'L'}(\mathbf{k},i\omega) = \sum_{j} \frac{u_{RL,j}(\mathbf{k})[u_{R'L',j}(\mathbf{k})]^{\dagger}}{i\omega_n + \mu - \epsilon_j(\mathbf{k})}. \tag{20}$$

The local Green's function is computed as

$$G_{RL,R'L'}(i\omega) = \sum_{\mathbf{k}} G_{RL,R'L'}(\mathbf{k},i\omega). \tag{21}$$

The higher-order moments can be calculated as products of the zeroth-order moment $\mathcal{M}^0_{Rl}$ and $\epsilon_j(\mathbf{k}) - \epsilon_{Rlv}$:

$$\begin{aligned} \mathcal{M}^1_{Rl} &= \sum_{j\mathbf{k}}^{occ.} \mathcal{M}^0_{Rl}[\epsilon_j(\mathbf{k}) - \epsilon_{Rlv}], \\ \mathcal{M}^2_{Rl} &= \sum_{j\mathbf{k}}^{occ.} \mathcal{M}^0_{Rl}[\epsilon_j(\mathbf{k}) - \epsilon_{Rlv}]^2. \end{aligned} \tag{22}$$

The charge density can be computed again from Eq. (18). Note that a cutoff at a finite frequency will lead to inaccurate Matsubara sums [69]. This can be corrected to some extent by taking the analytic tail of the Green's function into account [24,70].

C. Incorporating the local many-body self-energy

After the brief review of the energy-dependent and the energy-linearized basis sets we proceed with discussing a combination of these methods which allows to include the local DMFT self-energy in a charge self-consistent way. The DMFT maps self-consistently the many-body lattice problem to an impurity model, which can be solved by various many-body techniques and produces the impurity Green's function and the local self-energy [8]. The DMFT self-consistency condition is obtained by imposing that the impurity Green's function is the same as the lattice local Green's function.

In the EMTO+DMFT method [39], the self-consistent procedure starts with a guess for the local self-energy $\Sigma_{RL,RL'}(z)$ to be combined, through the Dyson equation, with the $\mathbf{k}$-resolved LDA Green's function (7), which represents the

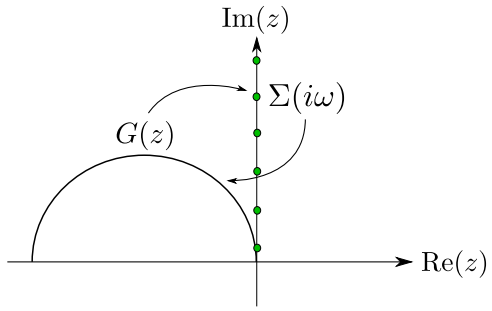

FIG. 1. Schematic picture of the complex energy contour and the Matsubara frequencies used in the EMTO+DMFT method [39]. Two Padé continuations are needed [Eqs. (24) and (26)], which are numerically ill-posed problems.

"noninteracting" lattice Green's function:

$$[G_{RL,R'L'}(\mathbf{k},z)]^{-1} = \left[G^{\mathrm{LDA}}_{RL,R'L'}(\mathbf{k},z)\right]^{-1} - \delta_{RR'}\Sigma_{RL,RL'}(z),$$
$$G_{RL,R'L'}(z) = \sum_{\mathbf{k}} G_{RL,R'L'}(\mathbf{k},z). \tag{23}$$

The local Green's function is extracted from Eq. (23) on the complex contour: $G_{RL,RL'}(z)$. Its matrix elements are analytically continued to the Matsubara frequencies:

$$G_{RL,RL'}(z) \xrightarrow{\text{Padé}} G_{RL,RL'}(i\omega). \tag{24}$$

In the next step, one has to construct the bath Green's function which specifies the impurity problem, which within EMTO+DMFT is computed from the analytically continued lattice local Green's function and the self-energy:

$$[\mathcal{G}_{RL,R'L'}(i\omega)]^{-1} = [G_{RL,R'L'}(i\omega)]^{-1} + \delta_{RR'}\Sigma_{RL,RL'}(i\omega). \tag{25}$$

The many-body problem is solved on the Matsubara axis, and the resulting self-energy is then analytically continued to the semicircular contour:

$$\Sigma_{RL,RL'}(i\omega) \xrightarrow{\text{Padé}} \Sigma_{RL,RL'}(z), \tag{26}$$

in order to close the LDA+DMFT loop. In Fig. 1 we illustrate the contours used in the EMTO+DMFT calculations. Accordingly, the self-consistency procedure requires two Padé analytic continuation [39,44] steps, that has to be controlled numerically.

In order to close the charge self-consistent loop, the LDA+DMFT path operator $g_{RL,R''L''}(z)$ is extracted from the interacting Green's function (23), while the real-space charge density is computed according to Eq. (9) substituting the LDA path operator with the corresponding LDA+DMFT path operator. The effective Kohn-Sham potential is obtained by solving the Poisson equation, and the scheme is iterated until self-consistency is achieved.

The LMTO method has previously been used as a choice for charge self-consistent basis sets. In particular, Pourovskii *et al.* [24] implemented an LDA+DMFT scheme in the LMTO-ASA method. In the case of LMTO-ASA, the LDA level Green's function is easily evaluated along the imaginary axis [Eq. (20)], and the self-energy $\Sigma(i\omega)$ is embedded via the Dyson equation to obtain the LMTO LDA+DMFT level Green's function. After performing the $\mathbf{k}$ sum, the bath Green's function is given similarly as in Eq. (25), and is given as input to the DMFT impurity solver. In order to close the charge self-consistent loop, the energy moments are computed as in Eqs. (19)–(22), with the exception that the Green's function in Eq. (19) is now on the LDA+DMFT level. The charge density is then computed from the energy moments as outlined in Eq. (18).

III. IMPLEMENTATION OF THE *z*MTO+DMFT METHOD

A. Motivation

In this section, we present a scheme that removes the need for the ill-posed analytic continuations (24) and (26) during the self-consistent loops. Two main ideas are used to achieve this: (i) the Green's function can be well approximated by linearization of the muffin-tin orbitals, and (ii) the charge density can be calculated by Matsubara summation.

1. Elimination of $G(z) \rightarrow G(i\omega)$: The benefit of a linearized basis set

A major difference between the Green's function within EMTO [Eq. (23)] and within LMTO-ASA [Eq. (16)] is that the latter can be easily evaluated for any energy once the potential parameters are known. The EMTO Green's function on the other hand requires the computation of the slope matrix and the solution of the radial Schrödinger equation at each energy point along the complex contour, and this is a numerically demanding task. The two Green's functions should be equivalent up to the error in the linearization imposed on the kink-cancellation condition [71], reflecting the error of the linearization of the muffin-tin basis set.

Based on the formal equivalence of these methods, and the similar results for the corresponding quantities (Green's functions and moments of these), we propose the following:

(i) The EMTO Green's function should be used for LDA calculations,

(ii) The LMTO Green's function should be used for DMFT calculations.

This replaces the need of a Padé approximant with a linearization of the basis set, a more well-controlled approximation.

To be specific, we outline the procedure: At each Kohn-Sham iteration, the kink matrix in Eq. (5) is set up for the complex energies along the contour, and the EMTO Green's function is used to solve the electronic structure problem as outlined in Sec. II A. The partial waves $\phi_{Rl}(r_R)$ are obtained by radially integrating the Schrödinger equation (3) for the linearization energy $z = \epsilon_{Rlv}$. From these partial waves, the LMTO potential parameters C_{Rl} and Δ_{Rl} can be obtained (see Ref. [72]). The LMTO Hamiltonian (12) is constructed and diagonalized, providing eigenvalues $\epsilon_j(\mathbf{k})$ and eigenvectors $u_{RL,j}(\mathbf{k})$. In the next step, the noninteracting local LMTO Green's function (21) is computed for the Matsubara frequencies $i\omega_n$. Correlation effects are generated by the interaction term, formally to be added to the noninteracting Hamiltonian H^{γ}. The explicit form of the four index Coulomb interaction matrix elements is discussed in Sec. IV. From the Green's function formulated on the Matsubara axis, the bath Green's

function (25) at the LMTO level is obtained, and passed into the DMFT many-body solver.

The error in the linearization can be assessed by comparing the density of states (DOS) arising from the EMTO and the LMTO Green's functions, both at LDA level (see left panel of Fig. 2). The EMTO method was iterated self-consistently for Ni (above left) and Fe (below left), using an *spd* basis set. The DOS was then evaluated from the imaginary part of Eq. (7) (black solid lines) and Eq. (16) (red dashed lines), along a horizontal contour close to the real energy axis. The curves are in good agreement with each other. The basis set linearization will introduce approximations, but these are easily controlled and can in principle be improved by including higher-order MTOs (the NMTO method [63]).

2. *Elimination of* $\Sigma(i\omega) \rightarrow \Sigma(z)$*: Charge density difference*

An essential step for the charge self-consistency of LDA+DMFT with the EMTO basis set [39] is the analytic continuation of the self-energy $\Sigma_{RL,RL'}(i\omega)$ back to the complex contour, which allows to update the path operator $g_{RL,RL'}(z)$ from which the real-space charge density (9) is computed. The correlation effects upon the real-space charge density have been analyzed in the previous LDA+DMFT implementation for Fe, Ni, and Cr [39]. In particular for Cr, LDA+DMFT charge density shows accumulation of *d* electrons due to correlation effects inside the muffin-tin spheres and a depletion of density in the interstitial region. To capture these correlation-induced *corrections* to the LDA charge density, it seems natural for the current implementation to propose the following scheme:

(i) The LDA charge density should be computed within EMTO, $n^{\rm EMTO}_{\rm LDA}(\mathbf{r})$, on the complex contour,

(ii) The DMFT charge density correction $\Delta n^{\omega}(\mathbf{r})$ should be computed within LMTO on the Matsubara axis.

To be specific, we outline the procedure: the LDA real-space charge density is calculated from the complex contour [see Eq. (9)]. Once the LMTO Green's function has been constructed on the Matsubara frequencies, the energy moments (19)–(22) are computed both on the LDA and the LDA+DMFT levels. This allows to evaluate the charge density $n^{\rm LMTO}_{\rm LDA(+DMFT)}(\mathbf{r})$ according to Eq. (18). The charge density difference $\Delta n^{\omega}(\mathbf{r})$ is then simply defined as

$$\Delta n^{\omega}(\mathbf{r}) \equiv n^{\rm LMTO}_{\rm LDA+DMFT}(\mathbf{r}) - n^{\rm LMTO}_{\rm LDA}(\mathbf{r}), \tag{27}$$

where the superscript of $\Delta n^{\omega}(\mathbf{r})$ emphasizes that this quantity is computed on the imaginary axis. The final LDA+DMFT real-space charge density $n(\mathbf{r})$ is obtained through

$$n(\mathbf{r}) \equiv n^{\rm EMTO}_{\rm LDA}(\mathbf{r}) + \Delta n^{\omega}(\mathbf{r}), \tag{28}$$

and is used to close the self-consistent cycle. Note that the charges computed along the Matsubara axis contain contributions from all orbitals, and not only from the correlated subset.

To assess the possible differences between the EMTO and LMTO charge densities, at the LDA level, we plot in Fig. 2 (right column) the valence charge density for Ni (Fe) in the upper (lower) panel. The EMTO charge densities (black solid lines) were iterated to self-consistency and evaluated according to Eq. (9). The LMTO charge (red dashed lines) was evaluated from the EMTO self-consistent potentials by computing first the energy moments of the LMTO Green's function (16) using the contour integration [36], and then applying Eq. (18). The charge densities are in a very good agreement.

3. *Total energy*

Within the Kohn-Sham scheme, the total-energy functional can be expressed as

$$E_{\rm DFT}[n(\mathbf{r})] = T_s[n(\mathbf{r})] + \int \frac{n(\mathbf{r}')n(\mathbf{r})}{|\mathbf{r}'-\mathbf{r}|} d\mathbf{r}' d\mathbf{r} + E_{xc}[n(\mathbf{r})] + \int V_{ext} n(\mathbf{r}) d\mathbf{r}, \tag{29}$$

where V_{ext} is the external ionic potential, E_{xc} is the exchange-correlation energy, and T_s is the Kohn-Sham single-particle kinetic energy. The square brackets indicate that the energy components are *functionals* of the density $n(\mathbf{r})$. For the proposed method, the charge density given as input is now computed on the LDA+DMFT level [Eq. (28)], as outlined in the previous section. A slight change in the expression of the kinetic energy

$$T_s[n(\mathbf{r})] \equiv \sum_j^{occ.} \int \Psi_j(\mathbf{r})(-\nabla^2)\Psi_j(\mathbf{r}) d\mathbf{r} = \sum_j^{occ.} \epsilon_j - \int n(\mathbf{r}) V_{\rm eff}(\mathbf{r}) d\mathbf{r} \tag{30}$$

has to reflect the change in the one-electron energies ϵ_j caused by the presence of the real part of the self-energy. Equation (1) was used for the second equality, of the above equation. In order to account for this change in the one-electron energies, the *difference* between the LDA and LDA+DMFT one-electron energies $\Delta\epsilon_j = \epsilon_j^{\rm LDA+DMFT} - \epsilon_j^{\rm LDA}$ is added to the expression for the kinetic energy. The total energy of a many-body system in the ground state includes also the Galitskii-Migdal contribution [68]. This contribution is added into all LDA+DMFT computations. Other formulations such as the variational Luttinger-Ward functional may give improved energies [8,20,73] but do not appear straightforward to implement in the present scheme. In the current implementation, the Galitski-Migdal energy contribution is computed on the Matusbara axis in the LMTO formulation:

$$E_{\rm GM} \equiv \frac{T}{2} {\rm Tr}_L \sum_n \sum_{\mathbf{k}} G_{RL,R''L''}(\mathbf{k}, i\omega_n) \Sigma_{R''L'',R'L'}(i\omega_n) e^{i\omega_n 0^+}, \tag{31}$$

where $G_{RL,R''L''}(\mathbf{k}, i\omega_n)$ is on the LMTO LDA+DMFT level. The final expression for the LDA+DMFT total energy is

$$E_{\rm LDA+DMFT}[n(\mathbf{r})] = E_{\rm LDA}[n(\mathbf{r})] + \Delta\epsilon_j + E_{\rm GM}. \tag{32}$$

The Kohn-Sham ϵ_j one-electron energies from the DFT (LDA) calculation already include some interaction effects through the Hartree and the exchange-correlation potential terms. Including the interactions explicitly in the form of the Hubbard Hamiltonian, some interaction contributions would be counted twice. Consequently, some double-counting correction has to be included. There is no universal solution to this problem, and most of the double-counting schemes are empirical. In

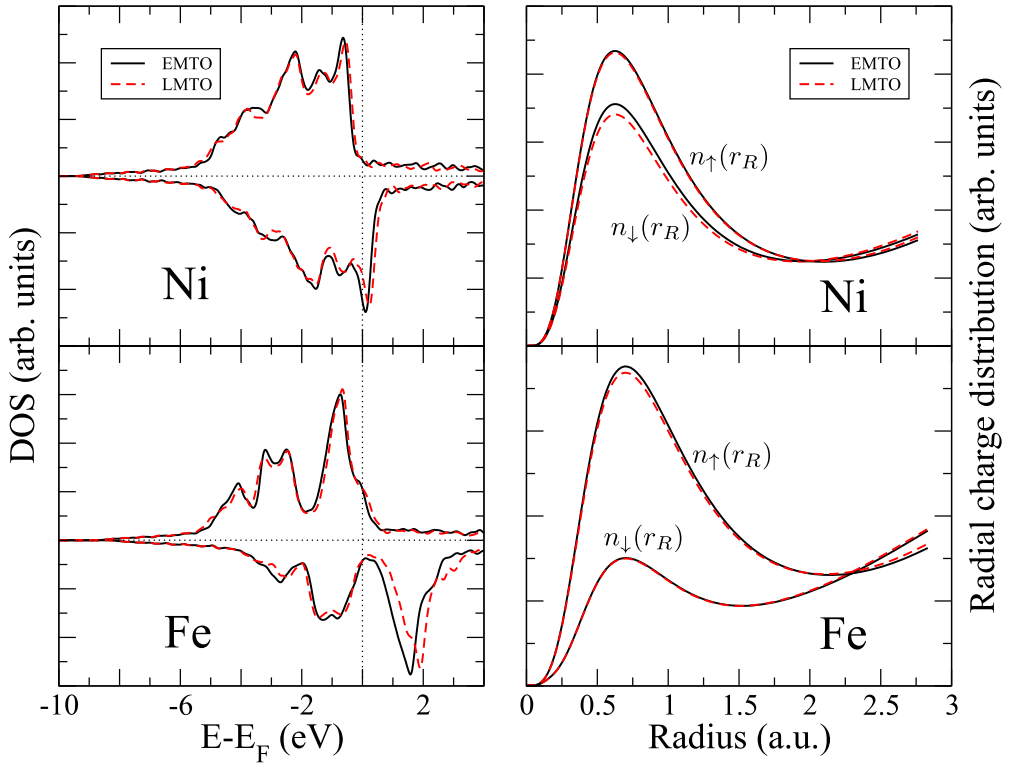

FIG. 2. Left panel: spin-resolved densities of states derived from EMTO (black solid line) and a linear approximation (red dashed line). (Top left) Majority and minority density of states of fcc Ni. (Bottom left) Majority and minority density of states of bcc Fe. Right panel: spin-resolved valence electron charge density for Ni (top right) and Fe (bottom right). The EMTO charge is plotted using black solid lines, while the charge stemming from linearization is shown with red dashed lines.

the present method we take over the schemes used in the previous implementation [39]; a detailed discussion is found in Ref. [74].

B. Flow diagram of the self-consistency calculation in *z*MTO+DMFT

The ideas presented in the previous section can be condensed in the following scheme that we call the *z*MTO+DMFT method (see Fig. 3):

(1) The Kohn-Sham iterations are initiated with a starting guess for the effective potential $V_{\text{eff}}(\mathbf{r})$ and the self-energy $\Sigma_{RL,RL'}(i\omega)$.

(2) The kink-cancellation equations are constructed for points along the complex contour, and the LDA level charge $n^{\text{EMTO}}_{\text{LDA}}(\mathbf{r})$ [Eq. (9)] is obtained by integrating along the contour. At this stage, the LMTO potential parameters are also computed from the partial waves.

(3) The Hamiltonian H^γ is constructed from the potential parameters from step (2) using Eq. (12), and the eigenvalue problem is solved.

(4) The noninteracting LDA Green's function (LMTO) is constructed according to Eq. (20) for the Matsubara frequencies from the Hamiltonian in step (3). The LMTO bath Green's function [Eq. (25)] is computed and iterated into the DMFT self-consistency loop, from which a new $\Sigma_{RL,RL'}(i\omega)$ is obtained.

(5) The $n^{\text{LMTO}}_{\text{LDA(+DMFT)}}(\mathbf{r})$ charges are obtained by Matsubara summation, and the difference $\Delta n^\omega(\mathbf{r})$ according to Eq. (27) is evaluated.

(6) The final LDA+DMFT charge density (28) is computed by adding $\Delta n^\omega(\mathbf{r})$ from step (6) to the DFT charge density from step (2).

(7) Return to step (2) until self-consistency in both the charge and self-energy is reached.

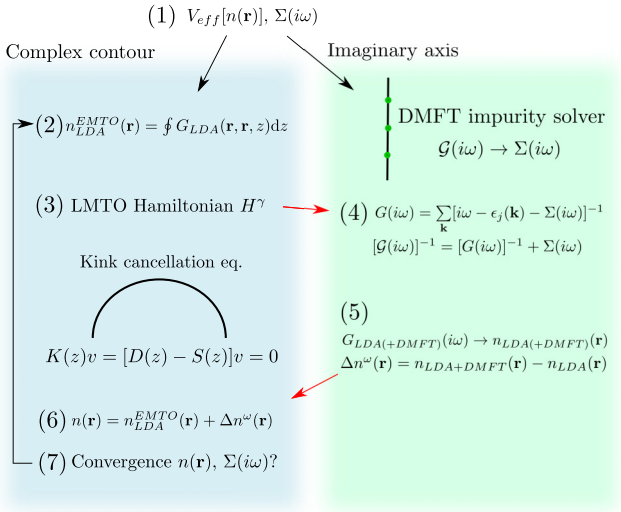

FIG. 3. Schematic flow diagram of the scheme. Note that within the cycle there is no analytic continuation needed since the quantities passed between the complex contour and the imaginary axis (red arrows) are energy independent (potential parameters and charge).

Once the self-consistency has been reached, observables such as the total energy (32) and spectral functions can be evaluated. Note that the spectral functions are evaluated on a horizontal contour slightly shifted away from the real axis. To analyze the self-energy along the real axis, a Padé approximant can be used. Note, however, that this does not affect the Kohn-Sham loops, and has to be carried out only once at the end, after self-consistency has been reached. In this case, it is also easy to identify spurious poles in the Padé approximant, as outlined in Ref. [48].

IV. RESULTS

To assess the implementation, electronic structure calculations have been performed according to the method proposed above. Transition metals and compounds in which the d-orbitals form the correlated basis set have been considered. For the DMFT impurity solver, a fluctuation exchange (FLEX) [75] type of approximation was used for the multiorbital case [70,76,77]. In contrast to the original formulation of FLEX [75], the spin-polarized T-matrix FLEX (SPTFLEX), used for the present calculations, treats the particle-particle and the particle-hole channels differently [70,76,77]. While the particle-particle processes are important for the renormalization of the effective interaction, the particle-hole channel describes the interaction of electrons with the spin fluctuations. In addition, the advantage of such a computational scheme is that the electron-electron interaction term can be considered in a full spin and orbital rotationally invariant form, viz., $\frac{1}{2}\sum_{i\{m,\sigma\}} U_{mm'm''m'''} c^{\dagger}_{im\sigma} c^{\dagger}_{im'\sigma'} c_{im'''\sigma'} c_{im''\sigma}$. Here, $c_{im\sigma}$ ($c^{\dagger}_{im\sigma}$) annihilates (creates) an electron with spin σ on the orbital m at the lattice site i. The Coulomb matrix elements $U_{mm'm''m'''}$ are expressed in the usual way [78] in terms of Slater integrals. Since specific correlation effects are already included in the exchange-correlation functional, so-called "double-counted" terms must be subtracted. To achieve this, we replace $\Sigma_\sigma(E)$ with $\Sigma_\sigma(E) - \Sigma_\sigma(0)$ [79] in all equations of the DMFT procedure [8]. Physically, this is related to the fact that DMFT only adds *dynamical* correlations to the DFT result [74].

A. Transition metals: Nickel and iron

Within the family of the late 3d transition metals, nickel and iron are known to show in their band structures signatures of electronic correlation [79]. Nickel is well known for a "6-eV satellite" in its photoemission spectra [80], while a similar satellite in iron is debated [25,81].

For both Fe and Ni, an spd basis was used, and the 4s and 3d states were treated as valence. The core electron levels were recalculated at each Kohn-Sham iteration (soft-core approximation). The kink-cancellation condition was set up for 16 energy points distributed around a semicircular contour with a diameter of 1 Ry, enclosing the valence band. The BZ integrations were carried out on an equidistant mesh with 285 **k**-points (for Fe) and 240 **k**-points (for Ni) in the irreducible BZ. For the exchange-correlation potential, the local spin density approximation with the Perdew-Wang parametrization [3] was used. For the DMFT impurity calculations, the Matsubara frequencies were truncated after 2048 frequencies, and the temperature was set to $T = 400$ K. The values for the Coulomb U and the exchange J parameters are discussed in connection with the presentation of the results in each case. The equations of state were obtained by fitting the energy-versus-volume data to a Birch-Murnaghan function [82]. The densities of state were computed along a horizontal contour shifted a distance $\delta = 0.02$ Ry away from the real-energy axis. At the end of the self-consistent calculations, to obtain the self-energy on a real-energy mesh, $\Sigma(i\omega)$ can be analytically continued into a horizontal contour by a Padé approximant constructed by the Thiele method [44].

In the top left part of Fig. 4, the LDA and LDA+DMFT density of states for Ni are presented. The volume was set to the experimental value (73.79 a.u.^{3}). The method compares well with previous DFT+DMFT studies employing the SPTFLEX impurity solver [25,39,40], and captures the main correlation effects of Ni such as the satellite formation and band narrowing. Note that the correlation effects are stronger in the majority spin channel (more pronounced satellite, more narrow bandwidth) than in the minority spin channel, which is common for the late 3d metals. For the case of $U = 3$ eV (blue line), the position of the "6-eV" satellite is at higher binding energy than in experiment. The value $U = 3$ eV has previously given the correct satellite position when a quantum Monte Carlo impurity solver was used [79], and the fact that the SPTFLEX solver overestimates the effect of correlation is thought to be due to the perturbative nature of the solver [84]. Recent spin-polarized positron annihilation experiments and LDA+DMFT calculations allowed to determine the value for the local electron-electron interaction strength in ferromagnetic nickel to the value of 2 ± 0.1 eV [85]. By decreasing the Coloumb parameter to $U = 2$ eV (red line), the satellite is shifted to lower binding energy, in better agreement with experiment, as found previously [84].

The top right part of Fig. 4 shows the equation of state of Ni as calculated within the method, for various values of the Coulomb parameters U and J. The effect of correlation can be seen to increase the equilibrium volume from the value given by the LDA (corresponding to $U = 0$, black line). The equilibrium volumes are given in Table I, together with the bulk moduli. As already mentioned in the discussion of the nickel DOS, the SPTFLEX solver overestimates the effect of correlation. This is seen for the equilibrium volume, where the commonly accepted value of $U = 3$ eV (blue line) overestimates the equilibrium volume. $U = 2$ eV (red line) gives a better agreement with the experimental volume. It should also be noted that the bulk modulus is softened as U is increased, which corrects for the overestimation made by the LDA functional.

Figure 4 shows the DOS (bottom left) and equation of state (bottom right) for bcc Fe, for the case of standard LDA ($U = 0$) and for $U = 1.7$ eV, $J = 0.9$ eV. Similar values of U and J have previously been successfully used to describe the photoemission spectra and energetics of iron [27,42,81]. The effect of correlation is seen to broaden the peaks in the DOS, and create a satellite structure at $\sim$7 eV binding energy, in agreement with previous SPTFLEX studies [25,27]. By including local correlation effects, the equilibrium volume is increased, similar as for Ni. This can be seen in the bottom right part of Fig. 4, where the equation of state is given.

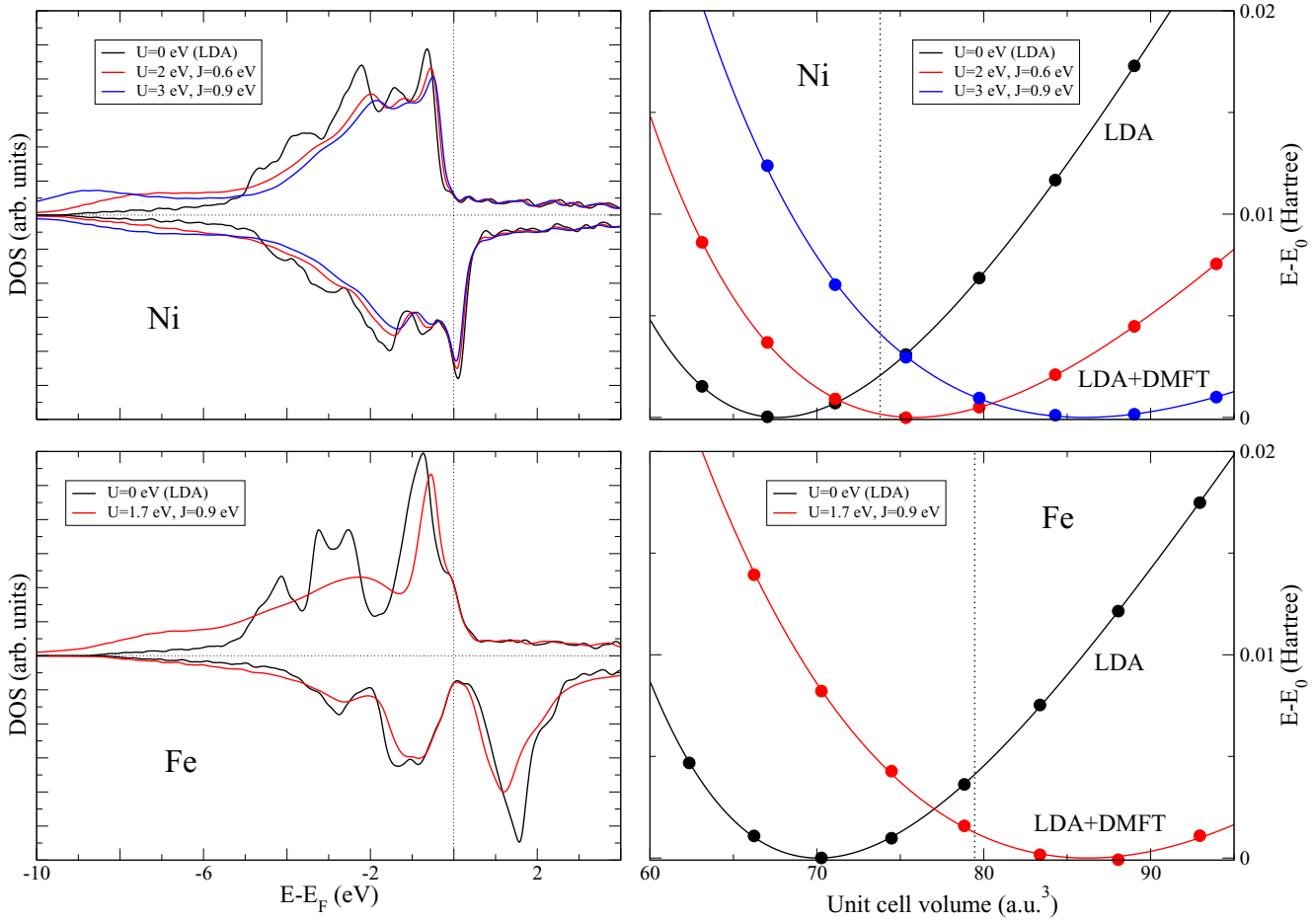

FIG. 4. Spin-resolved density of states (left) and equation of state (right) for nickel (top) and iron (bottom), for various values of the Coloumb parameters U and J. For Ni, the DOS was calculated for a unit-cell volume 73.79 a.u.^{3}, and for Fe the unit-cell volume was 78.84 a.u.^{3}. In the right panel, the dotted lines mark the experimental volumes.

The effect of correlation also reduces the bulk modulus (see Table I). The agreement between our results and the ones from Ref. [27] is very good; the slight differences are due to the spin-orbit coupling explicitly present in Ref. [27]. On the other hand, it is known that spin-orbit effects are quite small for Fe [86].

B. Iron aluminium

The stoichiometric intermetallic compound FeAl has attracted the interest of the electronic structure community mainly due to its magnetic properties. While FeAl is paramagnetic in experiment, LSDA calculations within density functional theory predict an ordered ferromagnetic ground state with a magnetic moment of about $\sim 0.7\mu_B$. Mohn *et al.* [87] showed that including the effect of the local Coulomb interaction U through the LDA + U method, the nonmagnetic state can be stabilized for a narrow range of U values. It was further argued that the reduction in the DOS at the Fermi level, caused by increasing U values, will favor the nonmagnetic state through the Stoner criteria. Petukhov *et al.* [74] pointed out the importance of dynamic effects by LDA+DMFT calculations of the spectral functions, showing that the nonmagnetic solution is stable within LDA+DMFT, and that the DOS is pinned to the Fermi level. Later on, Galler *et al.* [88] confirmed this, while also computing susceptibilities for FeAl within LDA+DMFT using a continuous-time quantum Monte Carlo (CT-QMC) impurity solver. None of the above previous LDA+DMFT studies presented total energies.

We have investigated the electronic structure of FeAl with our method, in order to evaluate the density of states and the total energy for volumes around the experimental value. FeAl crystallizes in the B2 (CsCl) structure, i.e., a simple cubic lattice with Fe at position (0,0,0) and Al at $(\frac{a}{2},\frac{a}{2},\frac{a}{2})$, where the experimental lattice constant is $a = 5.496$ a.u. [87] (note that also the value $a = 5.409$ a.u. is reported in the literature [89,90]). An *spd* basis was used, and a contour of diameter 1 Ry with 16 energy points was employed for the energy integrations. For the BZ integration, 286 **k**-points in the irreducible part was employed.

In the left part of Fig. 5, we present the nonmagnetic density of states for FeAl, computed assuming $U = 0$ eV (black line) and $U = 2$ eV (blue line). As pointed out in the previous studies [74,88], the increasing of the Coulomb U parameter, within LDA+DMFT, has little effect on the density of states at the Fermi level, in contrast to LDA + U calculations [87], while it leads to a band narrowing. This is an indication that spin fluctuations, which are included on a perturbative level in the SPTFLEX solver, changes the simple picture of Stoner instability.

TABLE I. Computed equilibrium volumes V_0 (a.u.^{3}) and bulk modulus B_0 (GPa) for fcc Ni and bcc Fe. Comparison is made with theoretical and experimental references. Data in parentheses next to a quantity are the relative difference between the quantity and the LDA ($U = 0$) value, $\delta x \equiv (x - x_{\mathrm{LDA}})/x_{\mathrm{LDA}}$. Experimental data taken from Ref. [83].

	LDA	$U = 2$ eV		$U = 3$ eV		
Ni	V_0	V_0	δV_0	V_0	δV_0	Expt.
This work	67.65	75.84	(0.12)	86.04	(0.27)	
FP-LMTO (Ref. [26])	67.88	76.20	(0.12)	89.48	(0.31)	73.79
KKR (Ref. [26])	66.86	76.28	(0.14)	85.53	(0.28)	
	B_0	B_0	δB_0	B_0	δB_0	
This work	259	162	(−0.37)	99	(−0.62)	
FP-LMTO (Ref. [26])	260	163	(−0.37)	84	(−0.68)	179
KKR (Ref. [26])	280	171	(−0.39)	132	(−0.53)	
Fe	LDA	$U = 1.7$ eV				Expt.
	V_0	V_0	δV_0			
This work	70.09	86.21	(0.23)			
FP-LMTO (Ref. [27])	70.49	87.06	(0.24)			79.46
	B_0	B_0	δB_0			
This work	253	124	(−0.51)			
FP-LMTO (Ref. [27])	234	90	(−0.62)			163

In the right panel of Fig. 5, our computed total energies for ferromagnetic and nonmagnetic FeAl are presented. In the case of LDA ($U = 0$, bottom right), the nonmagnetic total energy (black line) is never lower than the ferromagnetic total energy (red line), for all the studied volumes. In the lower volume range the ferromagnetic moment is lost, indicated by the coincidence of the two energy curves $\lesssim$70 a.u.^{3}. The fact that a ferromagnetic ground state is favored in LDA is in agreement with previous DFT studies [90]. The equilibrium volumes for the respective curves are 73.95 a.u.^{3} ($a = 5.288$ a.u.) for the ferromagnetic curve, and 73.62 a.u.^{3} ($a = 5.280$ a.u.) for the nonmagnetic curve, and hence the ferromagnetic and nonmagnetic lattice constants differ by $<1\%$ only. Previous DFT studies have found lattice constants of value $a = 5.397$ a.u. (TB-LMTO, nonlocal corrections to the LDA, Ref. [90]), $a = 5.364$ a.u. (TB-LMTO, Barth-Hedin parametrization of LDA, Ref. [89]), and $a = 5.330$ a.u. (full-potential linearized augmented Slater-type orbital method using LDA, Ref. [91]), using different basis sets and exchange-correlation functionals. The previously reported lattice constants are all larger than the current results, but are consistent given the fact that different basis sets and exchange-correlation functionals were used.

As local correlation effects are taken into account within LDA+DMFT ($U = 2$ eV, top right), the situation is reversed. In this case, the ferromagnetic solution is always higher in energy compared to the nonmagnetic solution, indicating that the nonmagnetic solution is the ground state for the whole volume range. For volumes $\lesssim$67 a.u.^{3}, the magnetic moment is lost, and the two curves coincide. The equilibrium volumes for the respective curves are 80.99 a.u.^{3} ($a = 5.451$ a.u.) for the ferromagnetic curve, and 82.67 a.u.^{3} ($a = 5.489$ a.u.) for the nonmagnetic curve, which is in good agreement with experiment.

Associating the analysis of the DOS and equation of state, we see that LDA+DMFT is able to explain the experimentally observed fact that FeAl is in a nonmagnetic ground state,

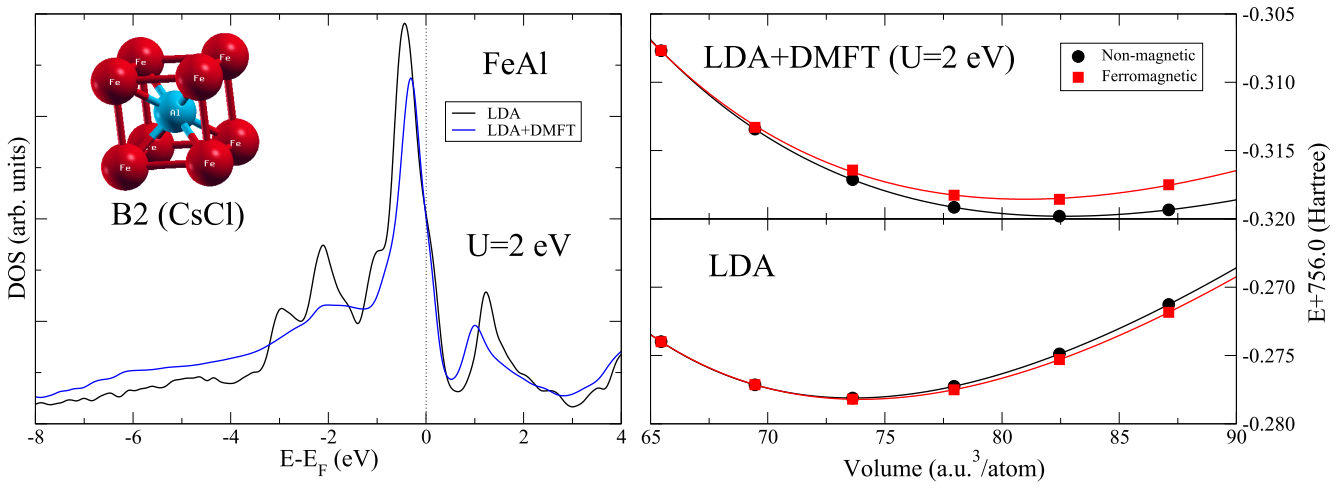

FIG. 5. Density of states (left) and equations of state (right) of FeAl.

while at the same time providing an equilibrium lattice constant in better agreement with experiment than the LDA. By investigating the DOS, the Stoner criterion (an increased DOS at E_F is leading to a magnetic instability) for ferromagnetism can be ruled out as an explanation for the magnetism in FeAl.

V. CONCLUSION AND OUTLOOK

In this paper, we have introduced a computational scheme for LDA+DMFT calculations, using Green's function methods. The method is able to describe correlated systems such as transition metals and compounds, and shows results in very good agreement with previous LDA+DMFT implementations. At the heart of the current implementation is the formulation of the LDA Green's function directly on the Matsubara axis, using the Lehmann representation in terms of the eigenvalues and eigenfunctions of the LMTO Hamiltonian. This simple procedure is essential for circumventing the analytical continuation of the Green's function from the complex contour to the Matsubara frequencies (Sec. III A 1). The real advantage of this construction appears in the computation of the charge density. Starting from the zeroth moment of the LMTO Green's function, the extension to higher-order moments becomes possible. From these moments, the real-space charge can be constructed. The difference between correlated and noncorrelated charge density allows for the self-consistency and in the same time circumvent the second analytical continuation, that of the self-energy from the Matsubara axis to the complex contour (Sec. III A 2). The idea to consider charge density differences between LDA and LDA+DMFT might also prove useful for Hamiltonian-based methods since the operation of subtraction could help in reducing systematic errors coming from the numerically difficult Matsubara sums.

By sidestepping the ill-posed analytic continuation problems, a numerically stable implementation is possible, at the minor cost of performing basis set linearization for the calculations along the imaginary axis.

Numerical results are presented for Fe and Ni. A direct numerical comparison between the imaginary part of the EMTO and the LMTO Green's functions along a horizontal contour close to the real axis is studied in Fig. 2. The agreement between the basis sets as well as for radially distributed real-space charge are found to be excellent. The zMTO+DMFT densities of states and total energy curves are then presented in Fig. 4, and are found to be in very good agreement with previous LDA+DMFT studies that were employing other basis sets. As a final example, the spectral functions and equations of state of the FeAl transition-metal compound is studied. Similarly, an excellent agreement is found when comparing to previous LDA+DMFT methods [74]. For a Coulomb interaction strength of magnitude $U = 2$ eV (on Fe in FeAl), the total energies for FeAl are seen to favor a nonmagnetic ground state, in accordance with experiment.

As an outlook, we propose several possibilities to extend the current zMTO+DMFT implementation. First, the downfolding of the linearized basis set can be included [24], in order to reduce the size of the minimal basis set even further. Second, the full-charge density (FCD) technique [58] applied to the EMTO method has previously provided accurate total energies for low-symmetry structures, while still keeping the efficiency of the spherical potential approximation (see Ref. [62]). The implementation of the FCD into the zMTO+DMFT method would make it possible to study the energetics of low-symmetry structures and anisotropic lattice distortions of correlated materials, which currently is work in progress. Finally, a major motivation is to enable a combination of the present method with the coherent-potential approximation [37], or with the typical medium theory for disorder [92]. This would provide a method that could handle strong correlation and disorder in alloy systems, including the problem of Anderson localization [92].

In conclusion, we have attempted to demonstrate by means of elementary examples that the current zMTO+DMFT, in conjunction with the perturbative SPTFLEX solver, can successfully describe the electronic structure and energetics of transition metals and their compounds. Even though the SPTFLEX solver is numerically simple due to its algebraic structure, it is still sufficiently rigorous to deal with correlated electrons in condensed matter. A more sophisticated implementation using a variant of the continuous-time quantum Monte-Carlo impurity solver is in progress.

ACKNOWLEDGMENTS

We greatly benefited from the discussions with D. Vollhardt and O. K. Andersen, whose advices are gratefully acknowledged. Financial support of the Deutsche Forschungsgemeinschaft through the Research Unit FOR 1346 is gratefully acknowledged. A.Ö. acknowledges helpful discussions with I. Di Marco. L.V. acknowledges financial support from the Swedish Research Council, the Swedish Foundation for Strategic Research, the Swedish Foundation for International Cooperation in Research and Higher Education, and the Hungarian Scientific Research Fund (OTKA Grants No. 84078 and No. 109570). We acknowledge computational resources provided by the Swedish National Infrastructure for Computing (SNIC) at the National Supercomputer Centre (NSC) in Linköping.

[1] P. Hohenberg and W. Kohn, Phys. Rev. **136**, B864 (1964).
[2] W. Kohn and L. J. Sham, Phys. Rev. **140**, A1133 (1965).
[3] J. P. Perdew and Y. Wang, Phys. Rev. B **45**, 13244 (1992).
[4] J. P. Perdew, K. Burke, and M. Ernzerhof, Phys. Rev. Lett. **77**, 3865 (1996).
[5] W. Metzner and D. Vollhardt, Phys. Rev. Lett. **62**, 324 (1989).
[6] A. Georges, G. Kotliar, W. Krauth, and M. J. Rozenberg, Rev. Mod. Phys. **68**, 13 (1996).
[7] G. Kotliar and D. Vollhardt, Phys. Today **57**(3), 53 (2004).
[8] G. Kotliar, S. Y. Savrasov, K. Haule, V. S. Oudovenko, O. Parcollet, and C. A. Marianetti, Rev. Mod. Phys. **78**, 865 (2006).
[9] K. Held, Adv. Phys. **56**, 829 (2007).

[10] I. Leonov, N. Binggeli, D. Korotin, V. I. Anisimov, N. Stojić, and D. Vollhardt, Phys. Rev. Lett. **101**, 096405 (2008).
[11] I. Leonov, D. Korotin, N. Binggeli, V. I. Anisimov, and D. Vollhardt, Phys. Rev. B **81**, 075109 (2010).
[12] I. Leonov, V. I. Anisimov, and D. Vollhardt, Phys. Rev. B **91**, 195115 (2015).
[13] I. Leonov, Phys. Rev. B **92**, 085142 (2015).
[14] B. Amadon, F. Lechermann, A. Georges, F. Jollet, T. O. Wehling, and A. I. Lichtenstein, Phys. Rev. B **77**, 205112 (2008).
[15] B. Amadon, J. Phys.: Condens. Matter **24**, 075604 (2012).
[16] Z. Jian-Zhou, Z. Jia-Ning, D. Xiao-Yu, B. Yan, C. Ling-Cang, F. Zhong, and D. Xi, Chin. Phys. B **21**, 057106 (2012).
[17] H. Park, A. J. Millis, and C. A. Marianetti, Phys. Rev. B **89**, 245133 (2014).
[18] H. Park, A. J. Millis, and C. A. Marianetti, Phys. Rev. B **90**, 235103 (2014).
[19] C. Taranto, M. Kaltak, N. Parragh, G. Sangiovanni, G. Kresse, A. Toschi, and K. Held, Phys. Rev. B **88**, 165119 (2013).
[20] S. Y. Savrasov and G. Kotliar, Phys. Rev. B **69**, 245101 (2004).
[21] E. Pavarini, S. Biermann, A. Poteryaev, A. I. Lichtenstein, A. Georges, and O. K. Andersen, Phys. Rev. Lett. **92**, 176403 (2004).
[22] F. Lechermann, A. Georges, A. Poteryaev, S. Biermann, M. Posternak, A. Yamasaki, and O. K. Andersen, Phys. Rev. B **74**, 125120 (2006).
[23] B. Amadon, S. Biermann, A. Georges, and F. Aryasetiawan, Phys. Rev. Lett. **96**, 066402 (2006).
[24] L. V. Pourovskii, B. Amadon, S. Biermann, and A. Georges, Phys. Rev. B **76**, 235101 (2007).
[25] A. Grechnev, I. Di Marco, M. I. Katsnelson, A. I. Lichtenstein, J. Wills, and O. Eriksson, Phys. Rev. B **76**, 035107 (2007).
[26] I. Di Marco, J. Minár, S. Chadov, M. I. Katsnelson, H. Ebert, and A. I. Lichtenstein, Phys. Rev. B **79**, 115111 (2009).
[27] O. Grånäs, I. D. Marco, P. Thunström, L. Nordström, O. Eriksson, T. Björkman, and J. Wills, Comput. Mater. Sci. **55**, 295 (2012).
[28] K. Haule, Phys. Rev. B **75**, 155113 (2007).
[29] K. Haule, C.-H. Yee, and K. Kim, Phys. Rev. B **81**, 195107 (2010).
[30] M. Aichhorn, L. Pourovskii, V. Vildosola, M. Ferrero, O. Parcollet, T. Miyake, A. Georges, and S. Biermann, Phys. Rev. B **80**, 085101 (2009).
[31] M. Aichhorn, L. Pourovskii, and A. Georges, Phys. Rev. B **84**, 054529 (2011).
[32] S. Bhandary, E. Assmann, M. Aichhorn, and K. Held, Phys. Rev. B **94**, 155131 (2016).
[33] M. Aichhorn, L. Pourovskii, P. Seth, V. Vildosola, M. Zingl, O. E. Peil, X. Deng, J. Mravlje, G. J. Kraberger, C. Martins *et al.*, Comput. Phys. Commun. **204**, 200 (2016).
[34] C. Weber, D. D. O'Regan, N. D. M. Hine, M. C. Payne, G. Kotliar, and P. B. Littlewood, Phys. Rev. Lett. **108**, 256402 (2012).
[35] O. Gunnarsson, O. Jepsen, and O. K. Andersen, Phys. Rev. B **27**, 7144 (1983).
[36] H. L. Skriver and N. M. Rosengaard, Phys. Rev. B **43**, 9538 (1991).
[37] P. Soven, Phys. Rev. **156**, 809 (1967).
[38] R. Zeller, J. Deutz, and P. Dederichs, Solid State Commun. **44**, 993 (1982).
[39] L. Chioncel, L. Vitos, I. A. Abrikosov, J. Kollar, M. I. Katsnelson, and A. I. Lichtenstein, Phys. Rev. B **67**, 235106 (2003).
[40] J. Minár, L. Chioncel, A. Perlov, H. Ebert, M. I. Katsnelson, and A. I. Lichtenstein, Phys. Rev. B **72**, 045125 (2005).
[41] J. Minár, J. Phys.: Condens. Matter **23**, 253201 (2011).
[42] I. Leonov, A. I. Poteryaev, V. I. Anisimov, and D. Vollhardt, Phys. Rev. Lett. **106**, 106405 (2011).
[43] I. Leonov, V. I. Anisimov, and D. Vollhardt, Phys. Rev. Lett. **112**, 146401 (2014).
[44] H. J. Vidberg and J. W. Serene, J. Low Temp. Phys. **29**, 179 (1977).
[45] K. S. D. Beach, R. J. Gooding, and F. Marsiglio, Phys. Rev. B **61**, 5147 (2000).
[46] H. S. Wall, *Analytic Theory of Continued Fractions* (Chelsea, New York, 1948).
[47] G. A. Baker, *Essentials of Padé Approximants* (Academic Press, New York, 1975).
[48] A. Östlin, L. Chioncel, and L. Vitos, Phys. Rev. B **86**, 235107 (2012).
[49] J. Schött, I. L. M. Locht, E. Lundin, O. Grånäs, O. Eriksson, and I. Di Marco, Phys. Rev. B **93**, 075104 (2016).
[50] J. Nordström, J. Schött, I. L. Locht, and I. Di Marco, SoftwareX **5**, 178 (2016).
[51] L. Chioncel, H. Allmaier, E. Arrigoni, A. Yamasaki, M. Daghofer, M. I. Katsnelson, and A. I. Lichtenstein, Phys. Rev. B **75**, 140406 (2007).
[52] M. I. Katsnelson, V. Y. Irkhin, L. Chioncel, A. I. Lichtenstein, and R. A. de Groot, Rev. Mod. Phys. **80**, 315 (2008).
[53] A. Östlin, W. H. Appelt, I. Di Marco, W. Sun, M. Radonjić, M. Sekania, L. Vitos, O. Tjernberg, and L. Chioncel, Phys. Rev. B **93**, 155152 (2016).
[54] F. Beiuşeanu, C. Horea, E.-V. Macocian, T. Jurcuţ, L. Vitos, and L. Chioncel, Phys. Rev. B **83**, 125107 (2011).
[55] L. Chioncel, C. Morari, A. Östlin, W. H. Appelt, A. Droghetti, M. M. Radonjić, I. Rungger, L. Vitos, U. Eckern, and A. V. Postnikov, Phys. Rev. B **92**, 054431 (2015).
[56] A. Östlin and L. Vitos, Phys. Rev. B **84**, 113104 (2011).
[57] A. Östlin, I. Di Marco, I. L. M. Locht, J. C. Lashley, and L. Vitos, Phys. Rev. B **93**, 094103 (2016).
[58] L. Vitos, J. Kollár, and H. L. Skriver, Phys. Rev. B **49**, 16694 (1994).
[59] O. K. Andersen, O. Jepsen, and G. Krier, *Lectures on Methods of Electronic Structure Calculation* (World Scientific, Singapore, 1994).
[60] L. Vitos, H. L. Skriver, B. Johansson, and J. Kollár, Comput. Mater. Sci. **18**, 24 (2000).
[61] L. Vitos, Phys. Rev. B **64**, 014107 (2001).
[62] L. Vitos, *Computational Quantum Mechanics for Materials Engineers* (Springer, London, 2010).
[63] O. K. Andersen and T. Saha-Dasgupta, Phys. Rev. B **62**, R16219 (2000).
[64] O. K. Andersen, Phys. Rev. B **12**, 3060 (1975).
[65] O. K. Andersen, O. Jepsen, and M. Sob, *Electronic Band Structure and Its Applications* (Springer, Berlin, 1986).
[66] O. K. Andersen and O. Jepsen, Phys. Rev. Lett. **53**, 2571 (1984).
[67] P. Weinberger, *Electron Scattering Theory for Ordered and Disordered Matter* (Clarendon Press, Oxford, 1990).
[68] A. L. Fetter and J. D. Walecka, *Quantum Theory of Many-Particle Systems* (McGraw-Hill, New York, 1971).

[69] D. M. C. Nicholson, G. M. Stocks, Y. Wang, W. A. Shelton, Z. Szotek, and W. M. Temmerman, Phys. Rev. B **50**, 14686 (1994).
[70] L. V. Pourovskii, M. I. Katsnelson, and A. I. Lichtenstein, Phys. Rev. B **72**, 115106 (2005).
[71] R. Tank and C. Arcangeli, Phys. Status Solidi B **217**, 89 (2000).
[72] H. L. Skriver, *The LMTO Method* (Springer, Berlin, 1984).
[73] K. Haule and T. Birol, Phys. Rev. Lett. **115**, 256402 (2015).
[74] A. G. Petukhov, I. I. Mazin, L. Chioncel, and A. I. Lichtenstein, Phys. Rev. B **67**, 153106 (2003).
[75] N. E. Bickers and D. J. Scalapino, Ann. Phys. (NY) **193**, 206 (1989).
[76] A. I. Lichtenstein and M. I. Katsnelson, Phys. Rev. B **57**, 6884 (1998).
[77] M. I. Katsnelson and A. I. Lichtenstein, J. Phys.: Condens. Matter **11**, 1037 (1999).
[78] M. Imada, A. Fujimori, and Y. Tokura, Rev. Mod. Phys. **70**, 1039 (1998).
[79] A. I. Lichtenstein, M. I. Katsnelson, and G. Kotliar, Phys. Rev. Lett. **87**, 067205 (2001).
[80] A. Liebsch, Phys. Rev. Lett. **43**, 1431 (1979).
[81] J. Sánchez-Barriga, J. Fink, V. Boni, I. Di Marco, J. Braun, J. Minár, A. Varykhalov, O. Rader, V. Bellini, F. Manghi *et al.*, Phys. Rev. Lett. **103**, 267203 (2009).
[82] F. Birch, Phys. Rev. **71**, 809 (1947).
[83] D. A. Young, *Phase Diagrams of the Elements* (University of California Press, Berkeley, 1991).
[84] M. I. Katsnelson and A. I. Lichtenstein, Eur. Phys. J. B **30**, 9 (2002).
[85] H. A. Ceeh, J. A. Weber, P. Böni, M. Leitner, D. Benea, L. Chioncel, H. Ebert, J. Minr, D. Vollhardt, and C. Hugenschmidt, Sci. Rep. **6**, 20898 (2016).
[86] O. Eriksson, B. Johansson, R. C. Albers, A. M. Boring, and M. S. S. Brooks, Phys. Rev. B **42**, 2707 (1990).
[87] P. Mohn, C. Persson, P. Blaha, K. Schwarz, P. Novák, and H. Eschrig, Phys. Rev. Lett. **87**, 196401 (2001).
[88] A. Galler, C. Taranto, M. Wallerberger, M. Kaltak, G. Kresse, G. Sangiovanni, A. Toschi, and K. Held, Phys. Rev. B **92**, 205132 (2015).
[89] V. Sundararajan, B. R. Sahu, D. G. Kanhere, P. V. Panat, and G. P. Das, J. Phys.: Condens. Matter **7**, 6019 (1995).
[90] N. I. Kulikov, A. V. Postnikov, G. Borstel, and J. Braun, Phys. Rev. B **59**, 6824 (1999).
[91] R. E. Watson and M. Weinert, Phys. Rev. B **58**, 5981 (1998).
[92] H. Terletska, Y. Zhang, L. Chioncel, D. Vollhardt, and M. Jarrell, Phys. Rev. B **95**, 134204 (2017).